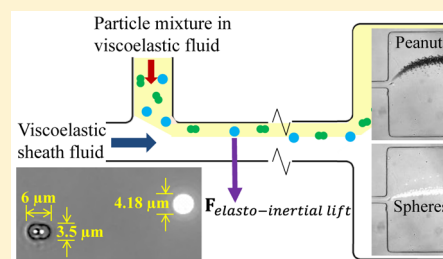# Elasto-Inertial Pinched Flow Fractionation for Continuous Shape-Based Particle Separation

Xinyu Lu and Xiangchun Xuan*

Department of Mechanical Engineering, Clemson University, Clemson, South Carolina 29634-0921, United States

S *Supporting Information*

ABSTRACT: Shape is an important passive marker in label-free particle and cell separation for chemical, biomedical, and environmental applications. We demonstrate herein a continuous-flow shape-based separation of spherical and peanut-shaped rigid particles of equal volume (or equivalent spherical diameter) via elasto-inertial pinched flow fractionation (eiPFF). This microfluidic technique exploits the shape dependence of the flow-induced elasto-inertial lift (and hence the cross-stream migration) in viscoelastic fluids to increase the displacement of a sheath flow-focused particle mixture for a high-purity separation. The parametric effects on this shape-based particle separation via eiPFF are systematically investigated in terms of five dimensionless numbers. It is found that the separation is strongly affected by the flow rate, fluid elasticity, and channel aspect ratio. Interestingly, the elasto-inertial deflection of the peanut particles can be either greater or smaller than that of equally volumed spherical particles. This phenomenon is speculated to correlate with the rotational effects of peanut particles.

$\bullet$hape is a fundamental property of particles and cells that can influence their interactions with the environment and determine their functional capabilities[1] and can be an important factor for characterizing cellular biospecies. For instance, prokaryotes are classified into different groups by shape such as rod-shaped, spiral-shaped, and spherical ones.[2] Shape has been found to play a significant role in phagocytosis where macrophages internalize pathogens and airborne particles of various shapes.[3] It can also be used to identify cell cycle stages. For example, budding yeasts undergo shape changes from spheres to bispherical twins or larger aggregates during cell division.[4] Moreover, shape is a good indicator of cell states that can provide useful information for disease diagnostics. It has been long known that the shape change of red blood cells is often accompanied by a disease such as sickle-cell disease[5] or malaria.[6] Therefore, shape is an important intrinsic marker for label-free cell and particle sorting, which may find applications in pathogen isolation from biological fluids for disease diagnostics, classification of environmental bacteria, and elimination of aggregates from synthesized particles etc.

A variety of microfluidic techniques have thus far been demonstrated to separate particles and cells in continuous flows.[7,8] However, the majority of these techniques are focused on particle separation by size.[9,10] Only until very recently has the particle shape been exploited as a passive sorting marker in a limited number of studies. Sugaya et al.[11] exploited the dissimilar rotation at fluid branch points to separate spherical particles from nonspherical particles and single yeasts from budding yeasts. This hydrodynamic filtration[12] technique requires the use of a network of microchannels. Valero et al.[13] utilized multifrequency dielectrophoresis to synchronize yeast cell division, which requires the integration of in-channel microelectrodes and also a precise control of the medium

electric conductivity. Beech et al.[14] used deterministic lateral displacement[15] to classify morphologically altered red blood cells based on shape. This technique, which has also been investigated by Zeming et al.[16] for shape-based separation, requires the fabrication of a high-resolution array of posts. Masaeli et al.[17] utilized differential inertial focusing[18] to sort spheres and rods as well as yeast cells at various stages in a long straight microchannel. This separation relies on high-flow speed-induced inertial lift and is thus restricted from handling small amount of samples. Recently, our group has used curvature-induced dielectrophoresis (C-iDEP)[19−21] to separate particles by shape in an asymmetric double-spiral microchannel.[22] This electrokinetic method suffers from a low throughput and may be harmful to cells due to potential electrical damages.[23]

In this work we demonstrate the use of a recently developed size-based particle separation technique in viscoelastic fluids,[24,25] which we termed elasto-inertial pinched flow fractionation or eiPFF in short,[26] to continuously separate particles based on shape in straight rectangular microchannels. As illustrated by the schematic (not to scale) in Figure 1, eiPFF exploits the strong size dependence of the flow-induced elasto-inertial lift (and hence the cross-stream migration) to increase the displacement of a sheath flow-focused particle mixture for a significantly enhanced separation than the traditional steric effects-based PFF.[27,28] We hypothesize that the elasto-inertial lift-induced particle migrations in viscoelastic fluids are also a function of particle shape, which will be demonstrated in this
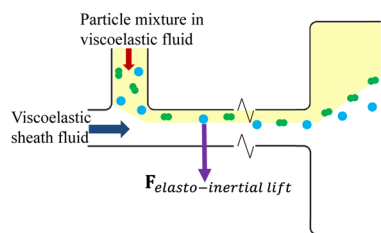
Figure 1. Schematic illustration (not to scale) of the mechanism for shape-based particle separation via eiPFF. The flow-induced elasto-inertial lift force (which can be simply viewed as a combination of elastic lift and inertial lift) in a viscoelastic fluid significantly increases the displacement of a sheath flow-focused mixture of spherical and peanut-shaped particles for a high-purity separation.

work by the continuous deflection and separation of spherical and peanut-shaped particles of equal volume. The observations will also be directly compared with those for particles suspended in a Newtonian fluid under identical experimental conditions. Moreover, a systematic study of the parametric effects such as flow rate, fluid elasticity, and channel aspect ratio will be carried out for a comprehensive understanding of the important factors that may impact the shape-based particle separation via eiPFF.

■ EXPERIMENTAL SECTION

Preparation of Particle Suspensions. Fluorescent spherical polystyrene particles of 4.18 μm diameter (Bangs Laboratories, Inc.) and plain peanut-shaped polystyrene particles of 3.5 μm diameter/6 μm length (Magsphere, Inc.) were used to demonstrate the shape-based separation. The peanut particles are obtained by fusing two 3.5 μm diameter spherical particles, whose overall volume was calculated to be 39.84 μm^3 using the geometry package in COMSOL. This volume corresponds to an equivalent spherical diameter of 4.23 μm, which deviates from that of the spherical particles by only 1.2%; see a zoom-in picture of both particles in Figure 2A. The
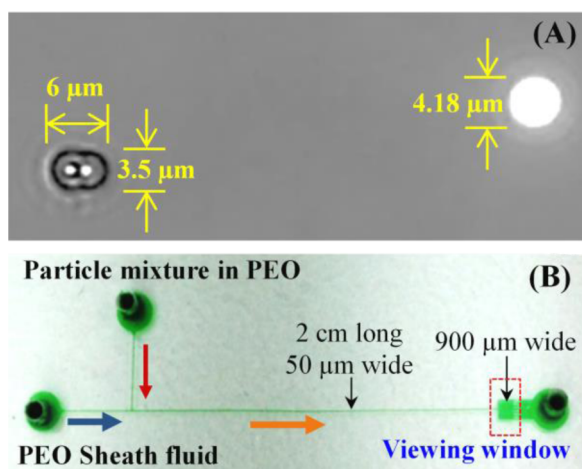

Figure 2. (A) Zoom-in view of one plain peanut-shaped particle (left, black) and one fluorescent spherical particle (right, white) of equal volume. (B) A top-view picture of the asymmetric T-shaped microchannel (filled with green food dye for clarity) used in experiments, where the block arrows indicate the flow directions and the dashed box highlights the 900 μm wide expansion region for visualizing particle separation. (Adapted from ref 26. Copyright 2015 American Chemical Society.)

two types of particles were mixed at a 1:1 ratio and resuspended in water-based Newtonian and non-Newtonian fluids to a final concentration of about 10^7 particles/mL. The Newtonian fluid was prepared by adding 0.5% (v/v) Tween 20 (Fisher Scientific) to water (Fisher Scientific) to reduce the influences of particle adhesions (to channel walls) and aggregations. The non-Newtonian fluids were prepared by dissolving poly-(ethylene oxide) (PEO) powder (Sigma-Aldrich U.S.A., molecular weight $M_w = 2 \times 10^6$ Da) into water at a range of concentrations. Tween 20 was also added to them at 0.5% (v/v) for a fair comparison of particle separation in between water and PEO solutions.

Table 1 lists the properties of the prepared PEO solutions at 20 °C (the operation temperature of all experiments). The zero-shear dynamic viscosities, η_0, of 500, 1000, and 3000 ppm PEO solutions were obtained from the paper of Rodd et al.,[29] which were originally measured in experiments. The viscosities of PEO solutions at other concentrations were calculated using the viscosity blending equation.[30] The overlap concentration, c^*, was calculated from the expression of Graessley,[31] $c^* = 0.77/[\eta]$ ppm, where the intrinsic viscosity, $[\eta] = 0.072M_w^{0.65} = 897$ mL/g, was given by the Mark−Houwink relation.[29] The effective relaxation times of the prepared PEO solutions were estimated from[32]

$$\lambda_e = 18\lambda_{Zimm}(c/c^*)^{0.65} \tag{1}$$

where λ_{Zimm} is the relaxation time predicted according to Zimm theory:[33]

$$\lambda_{Zimm} = F\frac{[\eta]M_w\eta_s}{N_A k_B T} \tag{2}$$

In the above the prefactor, $F = \sum_{i=1}^{\infty} i^{-3\nu} = 0.463$, was estimated from the Remann Z function using a solvent quality exponent, $\nu = 0.55$,[29] the solvent (i.e., water) viscosity η_s is equal to 1.0 mPa·s, N_A is the Avogadro's constant, k_B is the Boltzmann's constant, and $T = 293.15$ K is the absolute temperature. The prepared PEO solutions are in the dilute (under 500 ppm) or semidilute (beyond 500 ppm) regime, which exhibit a zero or a mild shear-thinning effect as reported in earlier studies.[34−37]

Experimental Setup. The standard soft lithography method was used to fabricate microchannels with poly-(dimethylsiloxane) (PDMS); see a top-view picture of the channel in Figure 2B. The details of the fabrication procedure are referred to Lu et al.[26,38] The asymmetric T-shaped microchannel has two 4 mm long side branches followed by a 2 cm long main branch with a uniform width of 50 μm. At the end of the main branch there is a 900 μm wide, 2 mm long expansion for enhancing and visualizing the particle separation. Four depths of channels were fabricated for the purpose of examining the effect of channel aspect ratio on particle separation, which are 15, 25, 40, and 100 μm, respectively. Infusion syringe pumps were used to drive the sheath fluid (New Era Pump Systems, Inc.) and particle mixture (KD Scientific). Particle motion was recorded through an inverted microscope (Nikon Eclipse TE2000U, Nikon Instruments) with a CCD camera (Nikon DS-Qi1Mc) at a frame rate of around 15 Hz. Fluorescent and bright-field lights were simultaneously used in order to visualize both the fluorescent spherical particles and the plain peanut-shaped particles. Images were postprocessed using the Nikon imaging software (NIS-Elements AR 3.22). Superimposed particle images were

Table 1. Properties of the PEO Solutions Used in Experiments (at 20 °C)

fluid properties	PEO concentration (c, ppm)								
	50	100	200	300	500	1000	1500	2000	3000
density ρ (g/cm^3)	1.0	1.0	1.0	1.0	1.0	1.0	1.0	1.0	1.0
zero-shear viscosity η_0 (mPa·s)	1.05	1.1	1.2	1.4	1.8	2.3	3.0	4.1	8.3
overlap concn c^* (ppm)	858	858	858	858	858	858	858	858	858
concn ratio c/c^*	0.06	0.12	0.23	0.35	0.58	1.17	1.75	2.33	3.50
Zimm relaxation time, λ_{Zimm} (ms)	0.34	0.34	0.34	0.34	0.34	0.34	0.34	0.34	0.34
effective relaxation time, λ_e (ms)	0.96	1.5	2.4	3.1	4.3	6.8	8.8	10.6	13.8

obtained by stacking a sequence of around 800 snapshot images with the maximum and minimum intensity projections for the fluorescent and plain particles, respectively.

DIMENSIONLESS NUMBERS

We study the parametric effects on particle separation via eiPFF in terms of five dimensionless numbers.[26] The Reynolds number is defined as the ratio of the inertial force to the viscous force

$$Re = \frac{\rho V D_h}{\eta_0} = \frac{2\rho Q}{\eta_0(w + h)} \tag{3}$$

where ρ is the fluid density, V is the average fluid velocity in a rectangular microchannel of width w and height h, $D_h = 2wh/(w + h)$ is the hydraulic diameter, and Q is the volumetric flow rate. The Weissenberg number measures the fluid elasticity effects and is defined as

$$Wi = \lambda_e \dot{\gamma} = \lambda_e \frac{2V}{w} = \frac{2\lambda_e Q}{w^2 h} \tag{4}$$

where $\dot{\gamma}$ is the average fluid shear rate in the microchannel. The elasticity number is defined as the ratio of fluid elasticity to inertia and is hence independent of the flow kinematics

$$El = \frac{Wi}{Re} = \frac{\lambda_e \eta_0(w + h)}{\rho w^2 h} \tag{5}$$

The flow rate ratio between the sheath fluid and particle mixture in the two side branches measures the sheath flow focusing performance in the main branch, which affects the particle deflection and dispersion at the channel expansion:

$$\alpha = \frac{Q_{sheath}}{Q_{particle}} \tag{6}$$

Note that the definitions of Re in eq 1 and Wi in eq 2 are both based on the total flow rate in the main branch of the microchannel, i.e., $Q = Q_{sheath} + Q_{particle}$. The channel aspect ratio is the channel width to height ratio:

$$AR = w/h \tag{7}$$

which, as recently reported,[39] affects the particle focusing position in non-Newtonian fluids through straight microchannels.

RESULTS AND DISCUSSION

Effects of Fluid Elasticity (Wi). Figure 3 compares the shape-based separation of fluorescent spherical particles and plain peanut particles in water (Figure 3A, $Wi = 0$) and 1000 ppm PEO solution (Figure 3B, $Wi = 6.35$) through a 25 μm deep microchannel (AR = 2.0). The sheath flow rate is 100 μL/h in both experiments, and the flow rate ratio between the
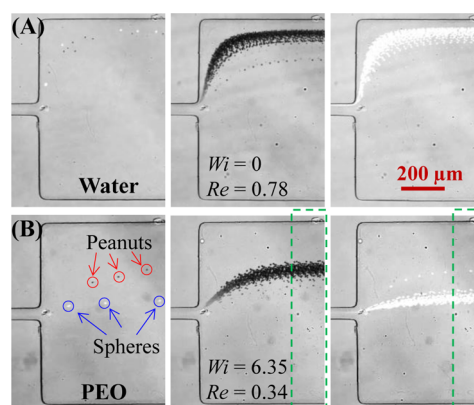

Figure 3. Comparison of shape-based separation of fluorescent spherical (white) and plain peanut-shaped particles (black) in water (A) and 1000 ppm PEO solution (B) through a 25 μm deep microchannel under the sheath flow rate of 100 μL/h and the flow rate ratio of 20. The images in the left, middle, and right columns are the snapshot images of both particles, superimposed images of peanut particles, and superimposed images of spherical particles at the channel expansion, respectively. The two dashed boxes in panel B highlight the regions to be used as cropped images in the following figures if applicable. The flow direction is from left to right in all images.

sheath fluid and particle mixture is fixed at $\alpha = 20$. In the Newtonian water solution, the spherical (appearing white) and peanut (appearing black) particles both move near the channel sidewall and overlap with each other without a visible separation; see the snapshot (left) and superimposed (middle for peanuts and right for spheres) images in Figure 3A. In contrast, they are both significantly deflected away from the sidewall by the flow-induced elasto-inertial (primarily elastic) lift in the viscoelastic PEO solution. Moreover, as demonstrated in Figure 2B, the exiting positions of spherical particles are much closer to the channel centerline and are thus clearly separated from the peanut particles with only very few particles scattered in between the two streams.

As suggested by the recent work from Masaeli et al.,[17] we tracked the orientation of peanut particles in the above two experiments using a high-speed camera (Photron SA-4, Motion Capture Technologies) at a frame rate of 3600/s. Figure 4A displays two superimposed images of single peanut particle traveling through the 50 μm wide main branch in water (top) and 1000 ppm PEO solution (bottom), respectively. The images were each obtained by superimposing every other frame of a short video, i.e., the time interval between neighboring particle positions on the images is fixed at 1/1800 s. The peanut particle in water seems to undergo a periodic three-dimensional rotation, both in-plane and out-of-plane, which has also been observed by Masaeli et al.[17] In contrast, the rotation in the PEO
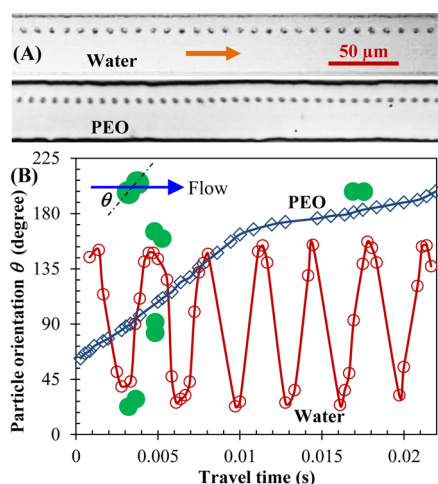
Figure 4. Comparison of the rotation of peanut particles in water and 1000 ppm PEO solution through a 25 μm deep microchannel under a sheath flow rate of 100 μL/h: panel A shows the superimposed images of a single peanut particle in water (top) and PEO (bottom), where the time interval between neighboring particle positions is 1/1800 s and the block arrow indicates the particle traveling direction; panel B shows the time-varied orientations of the long axis of peanut particles (markers) with respect to the flow direction (see the definition of angle θ on the schematic) in the two suspending fluids, which were estimated from the images in panel A (note that not all the particle orientations are included in the plot). The schematics of peanut particles on the plot are used to highlight the particle orientations at different angles. The solid lines are used to connect the markers only.

solution appears to be primarily in-plane and happens at an apparently lower speed than in water.

Figure 4B compares the time-varied orientations of the long axis of peanut particles (markers) in the two suspending fluids, which were estimated with respect to the flow direction from the top-view images in Figure 4A. The period of the peanut particle rotation in water is around 3 ms, which is consistent with the theoretical prediction of the orbit period, T_{orbit}, for an inertialess ellipsoid:[17,40]

$$T_{orbit} = \frac{2\pi}{\dot{\gamma}}\left(\alpha + \frac{1}{\alpha}\right) \qquad (8)$$

where $\dot{\gamma}$ is the local fluid shear rate, and α is the particle aspect ratio. Specifically, if it is viewed as an approximate ellipsoid, the peanut particle has an aspect ratio of $\alpha = 3.5/6$. The local shear rate can be estimated from the average flow velocity at 100 μL/h (i.e., 0.022 m/s) divided by the equivalent spherical diameter of the peanut particle (i.e., 4.23 μm), which gives $\dot{\gamma} = 5201$ s^{-1}. Substituting these parameters into eq 8 yields an orbit period of $T_{orbit} = 2.8$ ms for the peanut particle rotation in water, which is at least an order of magnitude shorter than that in PEO. Such a substantially extended period of particle rotation in a viscoelastic solution is consistent with the experimental observation of Bartram et al.,[41] who found a significant increase in the period of rotational rods in polyacrylamide (PAA) solution over that predicted by a Newtonian fluid-based theory. Moreover, this difference grows with increasing shear rate due to likely the existence of an elastic restoring torque opposing that from the viscous deformation of the fluid.[41]

It is also noticed in Figure 4B that the peanut particle in the PEO solution tends to travel with its long axis aligned toward the flow direction, i.e., 0° or 180° orientation. This can be viewed from the slope of the particle orientation versus time

curve, which indicates that the rotational speed is around 10° ms^{-1} and 2.4° ms^{-1} when the long axis of the peanut particle is perpendicular (i.e., 90° orientation) and parallel to the flow direction, respectively. Such a preferred parallel orientation renders the elasto-inertial lift force more dependent on the shorter dimension of the peanut particle (i.e., 3.5 μm), which is smaller than the diameter of the spherical particle (i.e., 4.18 μm). Furthermore, the peanut particle experiences a greater drag force due to its larger surface area,[42] yielding a smaller deflection than that of the spherical one as demonstrated in Figure 3.

Effects of Fluid Inertia (Re). Figure 5 shows the effect of flow rate (in terms of Re) on the shape-based separation in
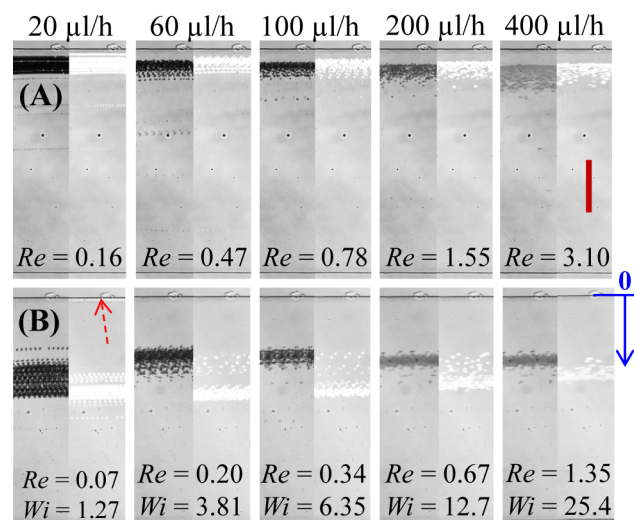

Figure 5. Cropped superimposed images (highlighted by the dashed boxes in Figure 3B) illustrating the effects of fluid elasticity (Wi) and inertia (Re) on the shaped-based separation of fluorescent spherical (white) and plain peanut (black) particles in water (A) and PEO solution (B) in a 25 μm deep microchannel. The sheath flow rate is varied from 20 to 400 μL/h from left to right while the flow rate ratio between the sheath fluid and particle mixture remains at $\alpha = 20$. The solid arrow on the right-most image in panel B indicates the reference point to which the particle stream positions in Figures 6, 9, and 10 were measured. The dashed arrow on the left-most image in panel B highlights a secondary equilibrium position at the channel corner for spherical particles in the PEO solution at a low flow rate. The scale bar on the right-most image in panel A represents 200 μm.

water (Figure 5A) and 1000 ppm PEO solution (Figure 5B) in a 25 μm deep microchannel. The sheath flow rate is varied from 20 to 400 μL/h while the flow rate ratio between the sheath fluid and particle mixture is fixed at $\alpha = 20$. In the Newtonian fluid, the equilibrium positions of spherical (white) and peanut (black) particles both appear to migrate away from the wall slightly with the increase of Re. This is a result of the increasing inertial lift force, though weak for small particles at Re of order 1, that acts to push particles away from walls.[43,44] However, as seen from Figure 5A, there is no particle separation observed in all the tested flow rates (up to 1 mL/h with Re = 7.76, image not shown). In contrast, the effect of Re on the equilibrium positions and separation of spherical/peanut particles in the PEO solution is much more complicated as demonstrated in Figure 5B. At the lowest sheath flow rate of 20 μL/h with Re = 0.07, each type of particle already attains a much larger deflection than that in water due to the action of the dominant elastic lift force at Wi = 1.27. While the deflection of spherical

particles (white) is apparently greater than that of peanut particles (black), the two particle streams still partially overlap with each other rendering the separation incomplete. Moreover, there seems to exist a secondary equilibrium position at the corner of the channel cross section for spherical particles (highlighted by the dashed arrow on the left-most image in Figure 5B) due to the negligible influence of inertial lift.[25,36,45] With the increase of Re, the deflection of spherical particles grows while that of peanut particles reduces, leading to an enhanced separation at 60 μL/h. Further increasing Re worsens the separation because the two types of particles tend to migrate toward a common equilibrium position due to the increasing dominance of inertial lift over elastic lift.

Figure 6 presents a quantitative comparison of the exiting positions of fluorescent spherical and plain peanut-shaped
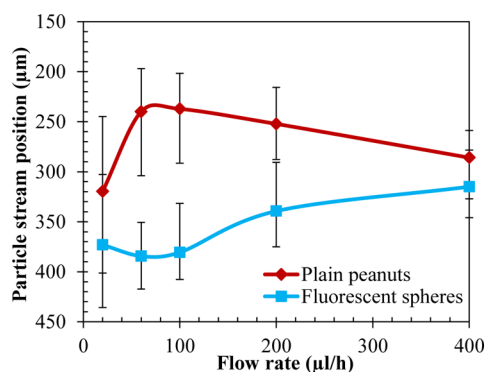

$\alpha = 5$ $\alpha = 10$ $\alpha = 20$ $\alpha = 33$ $\alpha = 50$

(A)

$Re = 0.38$ $Re = 0.35$ $Re = 0.34$ $Re = 0.33$ $Re = 0.33$
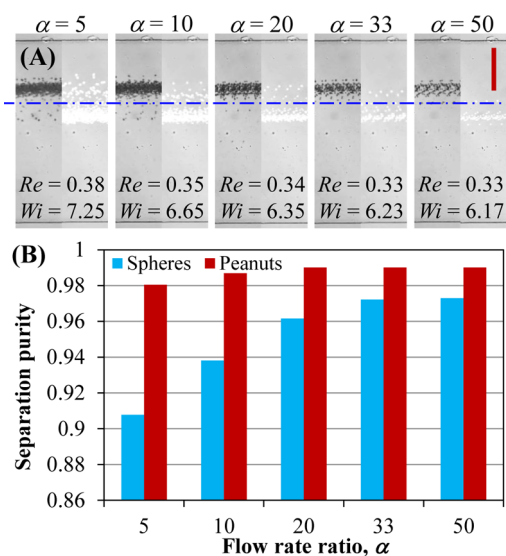$Wi = 7.25$ $Wi = 6.65$ $Wi = 6.35$ $Wi = 6.23$ $Wi = 6.17$

(B)

Figure 7. Flow rate ratio effect on the shape-based separation of fluorescent spherical (white) and plain peanut (black) particles via eiPFF in 1000 ppm PEO solution through a 25 μm deep microchannel under a constant 100 μL/h sheath flow rate: panel A shows the cropped superimposed images at the channel expansion, where the dashed-dotted line is right in the middle of the two separated particle streams; panel B shows the column plot for the measured separation purity (i.e., percentage) of spherical and peanut particles below and above the dashed-dotted line in panel A, respectively. The scale bar on the right-most image in panel A represents 200 μm.

Figure 6. Comparison of the exiting positions of fluorescent spherical and plain peanut particles at the expansion of the main branch in 1000 ppm PEO solution under various flow rates. All data points (symbols with error bars to encompass the span of each particle stream) were measured directly from the images in Figure 5B with reference to the top sidewall of the channel expansion as indicated by the solid arrow therein.

particles at the channel expansion. The data points were measured directly from the particle images in Figure 5B, where the top sidewall of the channel expansion was used as the reference point (see the solid arrow on the right-most image) and the center of each particle trace was used as the measuring point. The best particle separation seems to take place under a sheath flow rate of approximate 75 μL/h, where the deflections of spherical and peanut particles reach the maximum and minimum, respectively. The increase of flow rate beyond 100 μL/h appears to diminish the difference between the two types of particles due to the increasing role of the inertial lift force in eiPFF. The displacements of both particles from the channel sidewall seem to converge to a value of around 300 μm for flow rates greater than 400 μL/h, which is about one-third of the half-channel width away from the channel centerline. This particle focusing position seems consistent with that reported in a recent study,[39] where particles in a PEO solution were observed to migrate toward two positions that are each less than 0.4 times the half-channel width from the center. It is, however, different from the centerline equilibrium position for particles in Newtonian fluids through rectangular high-AR microchannels.[46,47]

Effects of Flow Rate Ratio, α. Figure 7A shows the flow rate ratio effect on the shape-based particle separation via eiPFF in 1000 ppm PEO solution through a 25 μm deep microchannel. The sheath flow rate is fixed at 100 μL/h

while the particle mixture flow rate is varied from 20 μL/h (i.e., $\alpha = 5$) to 2 μL/h (i.e., $\alpha = 50$). As the total flow rate in the main branch of the microchannel does not change significantly, Re slightly decreases from 0.39 to 0.33 with the increase of α. Meanwhile, Wi also decreases slightly from 7.25 to 6.17 to maintain the elasticity number at El = 18.8. Therefore, the elastic and inertial lift forces both remain nearly constant in the range of the tested α values, which explains why the deflections of spherical (white) and peanut (black) particles both remain almost unvaried in Figure 7A. However, a larger α indicates a better focusing of both types of particles at the T-junction of the microchannel (see Figures 1 and 2B),[24−28] which yields a smaller dispersion of either particles and hence an enhanced separation. The separation purity was determined by manually counting the percentages of spherical and peanut particles below and above the dashed-dotted line in Figure 7A, respectively, using the Nikon imaging software. This line was drawn right in the middle of the two separated particle streams because their center positions are both fixed in the range of the tested flow rate ratios. As seen from Figure 7B, the separation purity of either type of particles increases with α and is over 90% even for the smallest α of 5. Interestingly, the separation purity of peanut particles is higher than that of spherical particles at all the tested α values due partially to a smaller dispersion, for which the reason is currently unclear.

Effects of PEO Concentration (El). Figure 8 shows the PEO concentration effect on the shape-based particle separation via eiPFF in a 25 μm deep microchannel. The sheath flow rate and flow rate ratio are fixed at 100 μL/h and 20, respectively. The PEO concentration is increased from 0 (i.e., water with El = 0) to 3000 ppm (El = 138) with eight other concentrations in between. Due to the increase of viscosity at higher PEO concentrations (see Table 1), Re
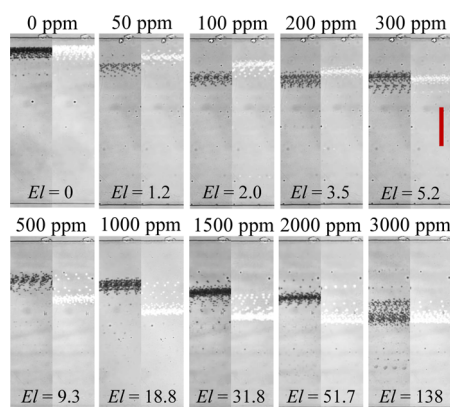
Figure 8. PEO concentration effect on the shape-based separation of fluorescent spherical (white) and plain peanut (black) particles via eiPFF in a 25 μm deep microchannel under a 100 μL/h sheath flow rate with a fixed flow rate ratio of 20. The scale bar on the right-most image of the top row represents 200 μm.

Figure 9. Comparison of the exiting positions of fluorescent spherical and plain peanut-shaped particles at the expansion of the main branch for different PEO concentrations. All data points (symbols with error bars to encompass the span of each particle stream) were measured directly from the images in Figure 8.

decreases from 0.78 to 0.09 indicating a continuously weakened inertial lift force. As illustrated in Figure 8, the deflections of fluorescent spherical (white) and plain peanut (black) particles both appear to increase with the PEO concentration due to the dominant elastic lift force. However, since the trend differs between the two types of particles, the particle separation exhibits an interesting concentration-dependent pattern. Specifically, peanut particles (black) obtain a greater deflection than spherical particles (white) when the PEO concentration is below 300 ppm. Within this range, the center-to-center separation gap between the two particle streams first increases with the PEO concentration until 100 ppm and then decreases to zero at 300 ppm. In contrast, when the PEO concentration is over 300 ppm, spherical particles (white) experience a larger deflection than peanut particles (black). However, similar to the lower concentration range (i.e., <300 ppm), the particle separation gap also undergoes a first-increase-then-decrease trend with the maximum taking place at around 1000 ppm. These interesting phenomena are speculated to be a consequence of the complicated PEO concentration effects on the rotation of peanut particles, which requires further intensive studies.

The effect of PEO concentration on particle deflection and separation in eiPFF can be viewed more clearly from the quantitative comparison of the exiting particle positions in Figure 9. The deflection of spherical particles quickly grows from 70 to 405 μm with the increase of PEO concentration until 1000 ppm, which then gradually levels off for concentrations over 1000 ppm with a seemingly equilibrium position near the channel centerline (i.e., particle stream position at 450 μm). In contrast, three regimes are observed for the deflection of peanut particles as the PEO concentration increases. From 0 to 100 ppm (El = 2.0), the deflection rapidly increases from 80 to 220 μm, which is faster than that of spherical particles as viewed from the slopes of the two curves in Figure 9. It then remains nearly constant at 225 μm ($\pm$5 μm) from 100 to 500 ppm (El = 9.3), which is about halfway from the channel centerline. Beyond that, the deflection of peanut particles follows a nearly linear relationship for PEO concentration up to 3000 ppm (the highest under test). It may be safe to assume that the spherical and peanut particles will eventually both migrate along the channel centerline at even higher PEO concentrations. Under the experimental
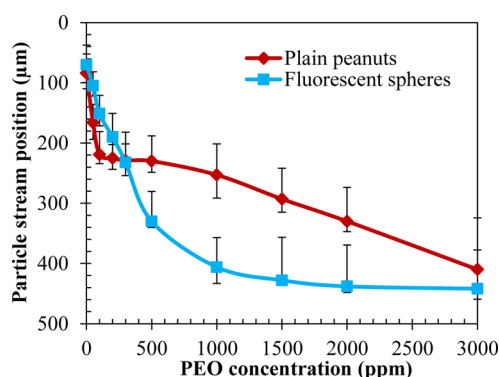
conditions, the largest separation gap between the two types of particles occurs in 1000 ppm PEO solution (El = 18.8).

Effects of Channel Aspect Ratio, AR. Figure 10 shows the channel aspect ratio effect on the separation of spherical
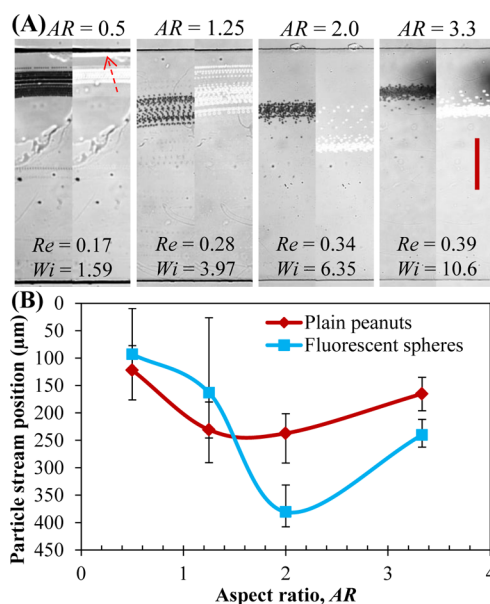

Figure 10. Channel aspect ratio effect on the shape-based separation of fluorescent spherical (white) and plain peanut (black) particles via eiPFF in 1000 ppm PEO solution under a 100 μL/h sheath flow rate with a fixed flow rate ratio of 20: panel A shows the cropped superimposed images at the channel expansion, where the dashed-dotted arrow highlights a secondary equilibrium position at the channel corner for spherical particles in a low-AR microchannel; panel B compares the exiting particle positions (symbols with error bars) at the expansion of the main branch. The scale bar on the right-most image in panel A represents 200 μm.

(white) and peanut (black) particles in 1000 ppm PEO solution through microchannels with depths of 100 μm (AR = 0.5), 40 μm (AR = 1.25), 25 μm (AR = 2.0), and 15 μm (AR = 3.3) from left to right. Under the fixed sheath flow rate of 100 μL/h and flow rate ratio of 20, Re and Wi both increase with AR while the latter grows faster, yielding an increasing El. In the 100 and 40 μm deep channels, the equilibrium position of peanut particles (black) is farther away from the wall than that

of spherical particles (white) as demonstrated in Figure 10A. Moreover, part of the spherical particles choose to move near the corner in the 100 μm deep channel, which is consistent with our recent observation in a similar microchannel.[26] The separation of the two types of particles is, however, weak in both of these low-AR channels due to the strong influence of particle dispersion. On the contrary, the deflection of spherical particles (white) surpasses that of peanut particles (black) in both the 25 and 15 μm deep channels. This is speculated to be due to the reduced rotational effects of the peanut particles, especially out-of-plane, in shallower microchannels, the consequence of which has been explained above (see Figure 4).

A similar switch in the particle deflections due to the variation of channel depth has also been observed in our recent study of particle separation by size via eiPFF.[26] The particle separation gets apparently better than in the two deeper microchannels due partially to the significantly reduced particle dispersion. Figure 10B compares the exiting positions of the two types of particles at the expansion of microchannels with different AR. The two curves indicate that the deflections of spherical and peanut particles become equal in a microchannel with AR $\approx$ 1.5, and the best separation is achieved at AR = 2.0. The nonmonotonic dependence on AR for the elasto-inertial deflection of spherical particles is absent from our recently demonstrated inertia-enhanced pinched flow fractionation (iPFF) in water.[48] It seems, however, consistent with the inertially focused spherical particles in straight rectangular microchannels at very high Re, where the equilibrium particle position can leave the channel center and shift toward the wall with the increase of AR.[47]

CONCLUSIONS

We have demonstrated a continuous separation of spherical and peanut particles of equal volume via a recently developed eiPFF technique.[26] This separation arises from the shape-dependent elasto-inertial lift-induced particle migration in viscoelastic fluids, which is speculated to correlate with the particle rotation effects. We have also performed a systematic experimental study of the parametric effects on such a label-free separation in terms of five dimensionless numbers, i.e., Re, Wi, El, α, and AR. It has been found that the separation is significantly affected by the flow rate and works effectively at Re of order 1. The separation purity is high for both the peanut and spherical particles even at a relatively small flow rate ratio α. Moreover, the separation has been found to show a strong dependence on both the fluid elasticity, El, and the channel aspect ratio, AR. These phenomena happen because the two types of particles follow apparently different trends when the PEO concentration or the channel depth is varied. Interestingly, the elasto-inertial deflection of peanut particles can be equal to or greater/smaller than that of spherical particles, depending on the values of El and AR. A similar correlation with AR has also been recently reported by our group for size-based particle separation via eiPFF.[26] To further verify the hypothesis of shape-dependent elasto-inertial lift force, we are currently fabricating ellipsoidal particles of various aspect ratios using the protocol reported earlier[3,17] for additional test of shape-based particle separation via eiPFF.

ASSOCIATED CONTENT

Ⓢ Supporting Information

The Supporting Information is available free of charge on the ACS Publications website at DOI: 10.1021/acs.analchem.5b03321.

> Movie at the T-junction of the microchannel for the shape-based particle separation in water (AVI)
> Movie at the outlet of the microchannel for the shape-based particle separation in water (AVI)
> Movie at the T-junction of the microchannel for the shape-based particle separation in 1000 ppm PEO solution (AVI)
> Movie at the outlet of the microchannel for the shape-based particle separation in 1000 ppm PEO solution (AVI)

AUTHOR INFORMATION

Corresponding Author
*E-mail: xcxuan@clemson.edu. Fax: +1 864 656 5630. Phone: +1 864 656 7299.

Notes
The authors declare no competing financial interest.

REFERENCES

(1) Jadhao, V.; Thomas, C. K; Olvera de la Cruz, M. *Proc. Natl. Acad. Sci. U. S. A.* **2014**, *111*, 12673−12678.
(2) Bauman, R. W. *Microbiology: With Diseases by Body System*, 4th ed.; Benjamin Cummings: San Francisco, CA, 2014; Chapters 4 and 11.
(3) Champion, J. A.; Mitragotri, S. *Proc. Natl. Acad. Sci. U. S. A.* **2006**, *103*, 4930−4934.
(4) Martin, S. *Cell Cycle* **2009**, *8*, 3643−3647.
(5) Ebert, E. C.; Nagar, M.; Hagspiel, K. D. *Clin. Gastroenterol. Hepatol.* **2010**, *8*, 483−489.
(6) Anstey, N. M.; Russell, B.; Yeo, T. W.; Price, R. N. *Trends Parasitol.* **2009**, *25*, 220−227.
(7) Lenshof, A.; Laurell, T. *Chem. Soc. Rev.* **2010**, *39*, 1203−1217.
(8) Plouffe, B. D.; Murthy, S. K. *Anal. Chem.* **2014**, *86*, 11481−11488.
(9) Shields, C. W., IV; Reyes, C. D.; Lopez, G. P. *Lab Chip* **2015**, *15*, 1230−1249.
(10) Gossett, D. R.; Weaver, W. M.; Mach, A. J.; Hur, S. C.; Tse, H. T.; Lee, W.; Amini, H.; Di Carlo, D. *Anal. Bioanal. Chem.* **2010**, *397*, 3249−3267.
(11) Sugaya, S.; Yamada, M.; Seki, M. *Biomicrofluidics* **2011**, *5*, 024103.
(12) Yamada, M.; Seki, M. *Anal. Chem.* **2006**, *78*, 1357−1362.
(13) Valero, A.; Braschler, T.; Rauch, A.; Demierre, N.; Barral, Y.; Renaud, P. *Lab Chip* **2011**, *11*, 1754−60.
(14) Beech, J. P.; Holm, S. H.; Adolfsson, K.; Tegenfeldt, J. O. *Lab Chip* **2012**, *12*, 1048−1051.
(15) Green, J. V.; Radisic, M.; Murthy, S. K. *Anal. Chem.* **2009**, *81*, 9178−9182.
(16) Zeming, K. K.; Ranjan, S.; Zhang, Y. *Nat. Commun.* **2013**, *4*, 1625.
(17) Masaeli, M.; Sollier, E.; Amini, H.; Mao, W.; Camacho, K.; Doshi, N.; Mitragotri, S.; Alexeev, A.; Di Carlo, D. *Phys. Rev. X* **2012**, *2*, 031017.
(18) Hur, S. C.; Choi, S. E.; Kwon, S.; Di Carlo, D. *Appl. Phys. Lett.* **2011**, *99*, 044101.

(19) Zhu, J.; Tzeng, T. J.; Xuan, X. *Electrophoresis* **2010**, *31*, 1382−1388.

(20) Zhu, J.; Xuan, X. *Biomicrofluidics* **2011**, *5*, 024111.

(21) DuBose, J.; Zhu, J.; Patel, S.; Lu, X.; Tupper, N.; Stonaker, J. M.; Xuan, X. *J. Micromech. Microeng.* **2014**, *24*, 115018.

(22) DuBose, J.; Lu, X.; Patel, S.; Qian, S.; Joo, S. W.; Xuan, X. *Biomicrofluidics* **2014**, *8*, 014101.

(23) Voldman, J. *Annu. Rev. Biomed. Eng.* **2006**, *8*, 425−454.

(24) Nam, J.; Lim, H.; Kim, D.; Jung, H.; Shin, S. *Lab Chip* **2012**, *12*, 1347−1354.

(25) Kang, K.; Lee, S. S.; Hyun, K.; Lee, S. J.; Kim, J. M. *Nat. Commun.* **2013**, *4*, 2567.

(26) Lu, X.; Xuan, X. *Anal. Chem.* **2015**, *87*, 6389−6396.

(27) Yamada, M.; Nakashima, M.; Seki, M. *Anal. Chem.* **2004**, *76*, 5465−5471.

(28) Mortensen, N. A. *Anal. Chem.* **2007**, *79*, 9240−9241.

(29) Rodd, L. E.; Scott, T. P.; Boger, D. V.; Cooper-White, J. J.; McKinley, G. H. *J. Non-Newtonian Fluid Mech.* **2005**, *129*, 1−22.

(30) Maples, R. E. *Petroleum Refinery Process Economics*; Pennwell Publishing: Tulsa, OK, 1993.

(31) Graessley, W. W. *Polymer* **1980**, *21*, 258−262.

(32) Tirtaatmadja, V.; Mckinley, G. H.; Cooper-White, J. J. *Phys. Fluids* **2006**, *18*, 043101.

(33) Rubinstein, M.; Colby, R. H. *Polymer Physics*; Oxford University Press Inc.: Oxford, U.K., 2003.

(34) Rodd, L. E.; Cooper-White, J. J.; Boger, D. V.; McKinley, G. H. *J. Non-Newtonian Fluid Mech.* **2007**, *143*, 170−191.

(35) Rodd, L. E.; Lee, D.; Ahn, K. H.; Cooper-White, J. J. *J. Non-Newtonian Fluid Mech.* **2010**, *165*, 1189−1203.

(36) Yang, S. Y.; Kim, J. Y.; Lee, S. J.; Lee, S. S.; Kim, J. M. *Lab Chip* **2011**, *11*, 266−273.

(37) Kim, J. Y.; Ahn, S. W.; Lee, S. S.; Kim, J. M. *Lab Chip* **2012**, *12*, 2807−2814.

(38) Lu, X.; Patel, S.; Zhang, M.; Joo, S. W.; Qian, S.; Ogale, A.; Xuan, X. *Biomicrofluidics* **2014**, *8*, 021802.

(39) Liu, C.; Xue, C.; Chen, X.; Shan, L.; Tian, Y.; Hu, G. *Anal. Chem.* **2015**, *87*, 6041−6048.

(40) Jeffery, G. B. *Proc. R. Soc. London, Ser. A* **1922**, *102*, 161−179.

(41) Bartram, E.; Goldsmith, H. L.; Mason, S. G. *Rheol. Acta* **1975**, *14*, 776−782.

(42) Happel, J.; Brenner, H. *Low Reynolds Number Hydrodynamics*; Noordhoff International Publishing: Leyden, Netherlands, 1973.

(43) Amini, H.; Lee, W.; Di Carlo, D. *Lab Chip* **2014**, *14*, 2739−2761.

(44) Martel, J. M.; Toner, M. *Annu. Rev. Biomed. Eng.* **2014**, *16*, 371−396.

(45) Del Giudice, F.; Romeo, G.; D'Avino, G.; Greco, F.; Netti, P. A.; Maffettone, P. L. *Lab Chip* **2013**, *13*, 4263−4271.

(46) Zhou, J.; Papautsky, I. *Lab Chip* **2013**, *13*, 1121−1132.

(47) Liu, C.; Hu, G.; Jiang, X.; Sun, J. *Lab Chip* **2015**, *15*, 1168−1177.

(48) Lu, X.; Xuan, X. *Anal. Chem.* **2015**, *87*, 4560−4565.